Plasmonically Enhanced Amorphous Silicon Photodetector with Internal Gain

Yugang Yu[†], Zihan Xu[†], Shilong Li, Alex Ce Zhang, Lujiang Yan, Zhaowei Liu and Yu-Hwa Lo*
Fellow, IEEE

Abstract—**Photodetectors made of amorphous materials enable low cost optical imaging and communications over non-semiconductor platforms. The key challenges are to improve efficiency, sensitivity, and frequency response. Using the localized surface plasmon resonance (LSPR) effect and an efficient carrier multiplication process, cycling excitation process (CEP), the plasmonically enhanced amorphous silicon photodetector (PEASP) with a thin (60 nm) absorption layer achieves a high external quantum efficiency with a record fast impulse response of 170 ps (FWHM). This approach offers the possibility of making detectors out of amorphous material for high frame rate imaging and optical communications in spite of the material's low carrier mobility.**

Index Terms—**Cycling excitation process (CEP), Localized surface plasmon resonance (LSPR), Plasmonically enhanced amorphous silicon photodetector (PEASP).**

I. INTRODUCTION

Photodetectors that convert optical signals into electrical currents are essential devices for imaging, sensing, and optical communications [1-2]. So far, inorganic crystalline semiconductors are the predominant material for photodetectors. Based on the operation wavelength, detectors are made of various types of crystalline semiconductors such as Si-, GaN-, and InGaAs-based materials. However, each material system requires a compatible crystalline semiconductor substrate that is nearly lattice-matched to the active layers of the detectors. The required high quality semiconductor substrates and epitaxial growth of active layers of detectors make photodetectors expensive to fabricate, costly to scale, and difficult to adapt to new platforms such as glass, ceramic or polymer substrates that become increasingly important for the emerging fields of internet of things (IOT), wearable electronics, flexible imaging and display, high frame rate cameras, underwater and free-space optical communications, etc. Therefore, there is a motivation to fabricate photodetectors on non-semiconductor substrate. Organic photodetectors, synthesized via low-cost solution-based methods on a non-semiconductor substrate, have been widely studied in this field [3-4]. In spite of promising results with organic semiconductor detectors, most organic semiconductor materials still suffer from poor stability, especially in environments with high temperature, moisture, light and oxygen [5-6]. To assure their reliability and performance in such common environments, complicated protection and encapsulation processes are required for organic detectors. In contrast, amorphous semiconductors such as amorphous silicon (a-Si) are stable with field-proven reliability for optoelectronic applications [7-8]. However, detectors made of a-Si face several issues that compromise the detector performance. The key performance limiting factors include high defect density, which leads to low EQE due to Shockley-Read-Hall carrier recombination, and very low electron and hole mobility, which leads to very low speed [9].

To address the speed problem and operate the device under low voltage, in this paper we demonstrate a detector with a very thin (60 nm) layer of a-Si as the light absorption layer. To overcome the problem of low external quantum efficiency due to the thin a-Si light absorption layer, two innovative approaches were employed. First, we used localized surface plasmon resonance (LSPR) effect from Au nanoparticles (NPs) to enhance the light-matter interactions. Second, we used an internal carrier multiplication mechanism in a-Si to amplify the photocurrent. The latter is referred to the cycling excitation process (CEP) reported in our earlier publication [10]. CEP is an internal photocurrent amplification mechanism found in (quasi)disordered materials such as heavily compensated p-n junction and amorphous Si [10-12]. These materials display strong carrier multiplication effect under high electric field due to the large amount of localized states in the bandtails. These bandtailed states can be excited into the mobile bands without the limit of k-selection rule that lowers the efficiency for conventional impact ionization. Aided by the plasmonically enhanced light-matter interaction and the CEP effect, a-Si detector can be an attractive alternative to organic semiconductors for light detection on non-semiconducting or compliant substrates.

II. EXPERIMENT

The device consists of a thin layer of un-doped a-Si sandwiched by two ITO electrodes. Between the a-Si layer and the bottom ITO electrode, there is a layer of randomly distributed Au NPs (40-nm in diameter) to enhance the electromagnetic (EM) field, and thus facilitating the light absorption of the thin a-Si layer via the LSPR effect [13-14]. We chose the dimension of Au nano-particles based on the localized surface plasmon resonance (LSPR) effect, fabrication process compatibility, and conditions in favor of CEP. In this paper,

The authors are with University of California, San Diego, La Jolla, CA 92092, USA. (email: ylo@ucsd.edu)
†: These authors contribute equally to this work.

we characterized the external quantum efficiency (EQE) and speed of the Plasmonically Enhanced Amorphous Silicon Photodetector (PEASP). To quantify the LSPR enhancement, we also characterized devices of the same structure without Au NPs.

A. Device Fabrication

The ITO on glass substrate was firstly solvent cleaned. To improve surface smoothness, ITO/glass substrate was soaked in KOH/isopropanol saturated solution for 2 hours at room temperature. Next, the substrate was rinsed with DI water and baked for 30 minutes. A layer of HMDS adhesion promoter was spin-coated onto the substrate. 1 mg/ml aqueous solution of Au NPs with a core diameter of 40 nm and PVP 40 kDa coating (NanoComposix) was diluted to 0.75 mg/mL with IPA and homogenized with 30 s of sonication. Then the 0.75 mg/mL Au NPs mixed solution was deposited on the substrate by drop coating at 55 °C, followed by 2-hour hard baking at 120 °C. The Au NPs coverage is around 25% measured by SEM. After Au NPs deposition, a 60 nm thick a-Si layer with 5% carbon doping was grown using PECVD. The growth temperature was 270 °C at the substrate and the flow rates were 450 sccm for silane (SiH4) and 24 sccm for methane (CH4). The a-Si film was hydrogen-loaded with H2 plasma. The first photo-lithography was performed to create photoresist patterns. A 130-nm thick ITO layer was sputtered on the patterned surface and lifted-off to define the top electrode. This ITO layer was also used as etch mask for plasma etch of a-Si in a self-aligned process. The ground contact pad was formed with a 200-nm thick sputtered Ti/Au layer on the bottom ITO electrode. The device schematic cross-section and the SEM image of Au NPs on the bottom ITO electrode are shown in Fig. 1 (a, b).
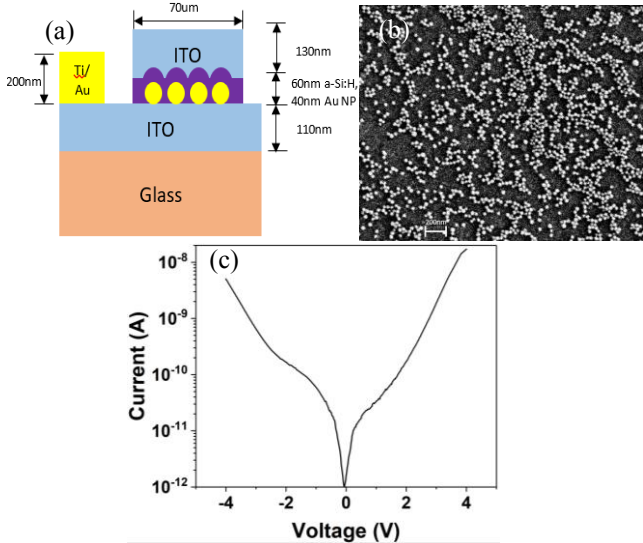

Fig. 1. Device structure and SEM image (a) Schematic diagram of device structure with material, function and thickness of each layer, (b) SEM image of Au NPs, (c) Device IV characteristic.

B. Characterization

The typical dark current-voltage characteristic of a 70 um diameter device with Au NPs is shown in Fig. 1 (c), measured by an Agilent B2912A precision source meter. To characterize device photoresponses, we used single mode fiber-pigtailed laser diodes modulated at 100 Hz and an SR865A lock-in amplifier to amplify the photocurrent of the device under different DC voltage bias. The laser

diodes were driven by a Thorlabs CLD1010 compact laser diode controller modulated by an Agilent 33600A series waveform generator. The measurement setup was controlled by LabView program.

To measure the high frequency characteristics of the devices, we used a high-speed ground-signal-ground (GSG) probe to make device contacts. For small-signal AC tests, the input laser light was modulated by an Agilent N5182A signal generator and the output current from the device was first amplified by an MITEQ AM-1300 low noise amplifier (27 dB voltage gain and 1.4 dB noise figure) and then measured by an HP 8594E spectrum analyzer. Limited by the response of the laser diodes and the bandwidth of Thorlabs CLD1010 laser driver, the small signal AC measurements were made over a range from 200KHz to 1GHz. To characterize the device properties at higher than 1 GHz frequency, we measured the impulse response using 375 nm and 639 nm wavelength picosecond pulsed lasers (PiLas) which produced 40 ps laser pulses at a 1 MHz repetition rate. The measurement setup is the same as small-signal AC test except that the output signal was measured by an Agilent DSO80604B Infiniium High Performance Oscilloscope.

C. Simulation Setup

The wavelength dependence of the real and imaginary parts of the refractive index, $n(\lambda)$ and $k(\lambda)$, for 5% C-doped a-Si was measured by Filmetrics, and used in EM simulations with the commercial software COMSOL Multiphysics 4.3, in order to calculate light absorption with or without Au NPs at different wavelength from the simulated electromagnetic field distribution. When the layer thickness is much smaller than the wavelength, the amount of light absorption is linearly proportional to the input intensity, and the absorption coefficient, $\alpha(\lambda)$, can be calculated from the imaginary part of the wave vector, $\mathbf{k}(\lambda)$, $\alpha(\lambda) = \frac{4\pi k(\lambda)}{\lambda}$. By performing the integration over the a-Si region, we have $\int_V dI(\vec{r}) = \int_V \alpha I(x, y, z) dx dy dz$, where x and y directions define the plane normal to the incident light. The quantum efficiency, η, is calculated by the adsorbed light power $\int_V dI(\vec{r})$ divided by the input power P_o as below,

$$\eta(\lambda) = \int_V dI(\vec{r})/P_o = \frac{n(\lambda)\alpha(\lambda)}{AE_o^2} \int_V |E(\vec{r})|^2 dx dy dz \quad (1)$$

where A is the area of the detector, λ is the wavelength in vacuum, E_0 and E are the incident and total electric field, respectively.

In these EM simulations, the periodicity of a single calculation cell is 70 nm along both the *x* and *y* directions, and the thickness of each layer is consistent with the actual device geometry shown in Fig. 1 (a). There is one Au NP with a diameter of 40 nm inside the calculation cell, so that the resultant fill factor (~25%) agrees with that of the measured result taken from SEM images, shown in Fig. 1 (b).

III. RESULTS

A. DC/Low Frequency Performance

We measured the device photoresponse at three wavelengths: red (639 nm), green (518 nm) and blue (488 nm) with incident light power of 350 pW, 80 pW and 70 pW, respectively. The bias dependent EQE for those three wavelengths is summarized in Fig. 2 (a, b, c). The EQE is determined by Eq. (2):

$$EQE = \frac{I_{ph}}{P_{in}} \times \frac{1240}{\lambda(nm)} \quad (2)$$

Where I_{ph} is the measured photocurrent, P_{in} is the input power and λ is the measured wavelength.

At all three wavelengths, the EQE of devices with Au NPs is appreciably greater than that of the devices without Au NPs, manifesting enhanced light adsorption of a-Si layer due to the LSPR effect. Notably for both devices with and without Au NPs, the EQE increases with voltage bias above 1 V due to the CEP amplification mechanism, which also contributes to high frequency response, to be elucidated later.
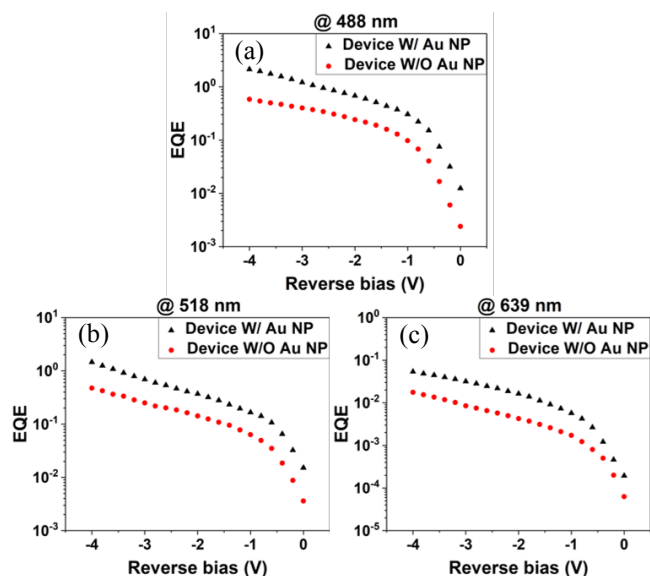

Fig. 2. EQE under bias (from -4 V to 0 V) at (a) 488 nm, (b) 518 nm, and (c) 639 nm wavelengths. Triangles are for the device with Au NPs and circles are for the device without Au NPs.

B. High Frequency Performance

One key performance limit for organic or amorphous semiconductor detectors is their frequency response due to the very low mobility. The slow response of the devices can limit their applications in high frame rate imaging, which is important for applications such as LIDAR for anonymous vehicle and optical communications. The small signal frequency response of the detectors at 518 nm wavelength, the desired wavelength for underwater communication [15], is shown in Fig. 3 (a). Compared with device without Au NPs, which has 3 dB cutoff frequency around 300 MHz, the detector with the help of LSPR achieves a bandwidth of over 1 GHz. This small signal modulation bandwidth is limited by the bandwidth of the 518 nm diode laser, and the actual device bandwidth can be significantly greater. Even with 1 GHz bandwidth, the speed is already more than 10 times faster than the best reported results of solution-processed organic semiconductor photodetectors [16]

To investigate the intrinsic device speed without the limitation of laser driver, the bandwidth of the device with Au NPs was also characterized by its impulse response using pulsed lasers at 375 nm and 639 nm wavelength. The pulse width of the laser sources is around 40 ps, and the impulse responses of the device with and without Au NPs at 375 nm and 639 nm are shown in Fig. 3 (b) and (c) respectively. Consistent with the results from small signal measurements, there is an obvious increase on the device speed induced by LSPR. The rise time for devices without Au NP is 240 ps at 375 nm, and its value is reduced to 85 ps for devices with Au NPs. At 639 nm wavelength, the device

rise time was reduced from 330 ps to 75 ps due to the incorporation of Au NPs. In terms of the full pulse width at half maximum (FWHM), devices with Au NPs achieve a FWHM of around 170 ps (FWHM) at both wavelengths, while the a-Si devices without Au NPs have a FWHM of 540 ps at 375 nm wavelength and 600 ps at 639 nm wavelength. Among all high-speed detectors made of amorphous or disordered materials [17-18], our devices show superior performance under low optical power and have low dark current, suitable for communications and imaging applications. Apart from the speed increase, the devices with Au NPs show significant QE enhancement due to LSPR effect in spite of their thin light absorption layer. The underlining physics about EQE and speed enhancements of the a-Si detectors with Au NPs will be discussed in the next section.
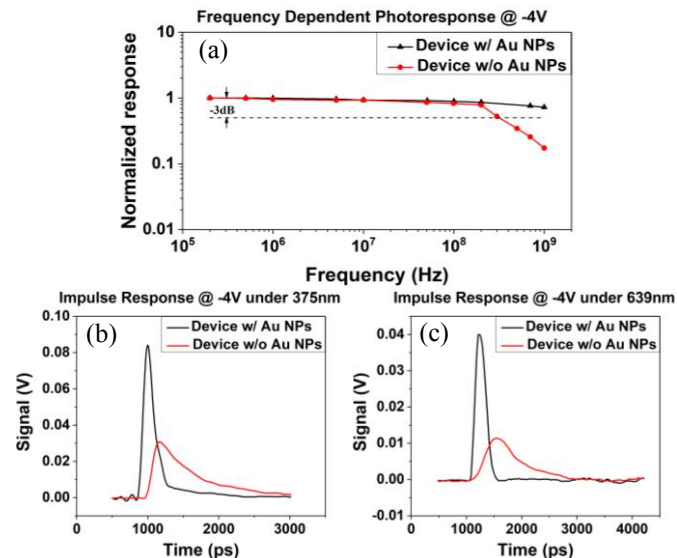

Fig. 3. High speed measurement results. (a) Frequency response of 518 nm for devices with and without Au NPs under -4 V, from 200 kHz to 1 GHz, (b) Impulse response to 40 ps laser pulses at 375 nm wavelength and 1 MHz repetition rate, (c) Impulse response to 40 ps laser pulses at 639 nm wavelength and 1 MHz repetition rate.

C. Simulation Results

The calculated electric fields at wavelengths of 488 nm, 518 nm, and 639 nm are shown in Fig. 4 (a, b, c), while a 3-D schematic of the a-Si active layer used in the EM simulations is given in Fig. 4(d) for clarity. The electric field in the a-Si active layer is concentrated near the surface of the embedded Au NP due to the LSPR, contributing to the enhancement of the absorption efficiency.

We use Eq. (1) to calculate light absorption at different wavelength from the simulated electromagnetic field distribution. To represent the enhancement due to Au nanoparticles, we use the ratio of the integrated square of the magnitude of electromagnetic field with and without Au nanoparticles, shown in Fig. 4 (e). By taking the QE ratio of devices with and without Au NPs, we obtain the QE enhancement factor caused by embedded Au NPs (Fig. 4 (f)). An improved absorption efficiency by factors of 1.6 to 3.8 from 450 nm to 700 nm is obtained owing to the LSPR near the Au NP. The result is in agreement with the experimental observation shown in Fig. 2 where the device with Au NPs under -2 V bias exhibits an improved EQE by factors of 2.62 at 488 nm, 2.51 at 518 nm, and 4.72 at 639 nm, respectively.
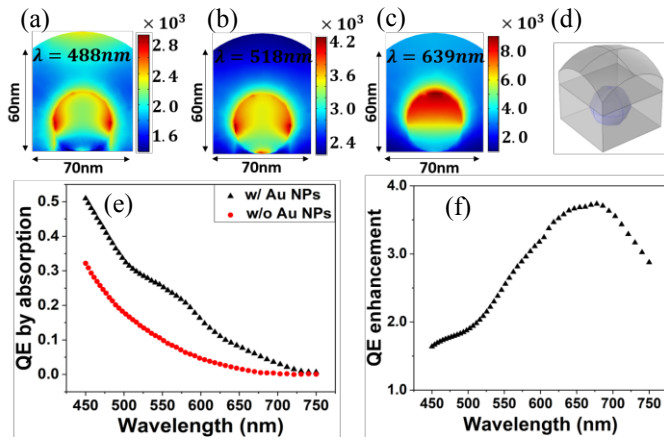
Fig. 4. 3D EM simulation results of electric field in the a-Si active layer and quantum efficiency enhancement by LSPR effect: (a) simulated electric field under 488 nm; (b) 518 nm; (c) 639 nm; (d) 3d structure of the a-Si layer with an Au NP; (e) wavelength dependent absorption with and without Au NP; (f) QE enhancement factor induced by Au NP

With the enhancement of electromagnetic field in a-Si near the Au NPs, the amount of the photo-generated electron-hole pairs in the a-Si active layers would be increased. In addition, the DC electric field under voltage bias is also expected to be enhanced in regions near the Au NPs, giving rise to a good match between the region of light absorption and the region of high E-field to rapidly drive the photogenerated electrons and holes towards their respective electrodes (cathode and anode). To illustrate this effect, the distribution of DC electric field was simulated and the results are shown in Fig. 5. Without the Au NP, the DC electric field in the a-Si active layer is uniformly distributed. In contrast, we found that the E-field near the upper half of the particle reaches a much higher level. Even in areas near the upper contact and farthest from the Au NP, the E-field exhibits a comparable value to the device without Au NPs. The EM field distributions in Fig. 4 and the DC electric field distributions in Fig. 5 support our hypothesis that the presence of Au NPs creates a good match between the distribution of the EM field and the DC electric field, which favors rapid transport of photogenerated carriers and results in higher frequency responses.
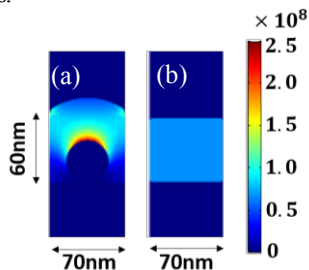

Fig. 5. DC electric field simulation in the a-Si active layer for (a) device with Au NPs, (b) device without Au NPs

IV. CONCLUSION

We have demonstrated that by using gold nanoparticles embedded in a thin amorphous silicon layer and an effective intrinsic photocurrent amplification mechanism, significant enhancement of the external quantum efficiency, detectivity, and frequency response of photodetectors can be achieved. The addition of Au NPs can enhance the external quantum efficiency by approximately a factor of 3. Moreover, CEP amplification mechanism allows achievement of high EQE even with a very thin absorption layer. Besides the

improvement of responsivity, the detector has shown a high speed in spite of the material's low electron and hole mobility. We have demonstrated a modulation bandwidth well above 1 GHz and a FWHM of 170 ps. Even though the device has a narrower spectral range of operation than a conventional device because of its thin a-Si:H layer that is essential to achieving high CEP gain and high frequency response, the design has been optimized for blue-green wavelength for applications such as underwater communications, air pollution detection, free-space optical communications, LIDAR, etc. Unlike semiconductor detectors that require high quality, single crystal, rigid substrates and expensive epitaxial growth, amorphous Si thin film detectors can be deposited on various substrates and fabricated in a simple, low cost, and highly scalable process to support emerging applications such as IoT, wearable electronics, flexible displays, autonomous vehicles, and more.

V. ACKNOWLEDGE

VI. REFERENCES

[1] Donati, Silvano. "Photodetectors: devices, circuits, and applications." (2001): 653.
[2] Konstantatos, Gerasimos, and Edward H. Sargent. "Nanostructured materials for photon detection." Nature nanotechnology 5.6 (2010): 391.
[3] Gong, Xiong, et al. "High-detectivity polymer photodetectors with spectral response from 300 nm to 1450 nm." Science325.5948 (2009): 1665-1667.
[4] Yao, Yan, et al. "Plastic Near-Infrared Photodetectors Utilizing Low Band Gap Polymer." Advanced Materials 19.22 (2007): 3979-3983.
[5] Asghar, M. I., et al. "Device stability of perovskite solar cells–A review." Renewable and Sustainable Energy Reviews 77 (2017): 131-146.
[6] Thomas, Simil, et al. "Improving the Stability of Organic Semiconductors: Distortion Energy versus Aromaticity in Substituted Bistetracene." Chemistry of Materials 28.23 (2016): 8504-8512.
[7] Carlson, David E., and Cristopher R. Wronski. "Amorphous silicon solar cell." Applied Physics Letters 28.11 (1976): 671-673.
[8] Cocorullo, Giuseppe, et al. "Amorphous silicon-based guided-wave passive and active devices for silicon integrated optoelectronics." IEEE Journal of selected topics in quantum electronics 4.6 (1998): 997-1002.
[9] Sakata, I., and Y. Hayashi. "Theoretical analysis of trapping and recombination of photogenerated carriers in amorphous silicon solar cells." Applied Physics A 37.3 (1985): 153-164.
[10] Yan, Lujiang, et al. "An amorphous silicon photodiode with 2 THz gain-bandwidth product based on cycling excitation process." Applied Physics Letters 111.10 (2017): 101104.
[11] Liu, Yu-Hsin, et al. "Cycling excitation process for light detection and signal amplification in semiconductors." Optical Sensing, Imaging, and Photon Counting: Nanostructured Devices and Applications 2016. Vol. 9933. International Society for Optics and Photonics, 2016.
[12] Hall, David, et al. "Approaching the Quantum Limit of Photodetection in Solid-State Photodetectors." IEEE Transactions on Electron Devices 64.12 (2017): 4812-4822.
[13] Link, Stephan, and Mostafa A. El-Sayed. "Optical properties and ultrafast dynamics of metallic nanocrystals." Annual review of physical chemistry 54.1 (2003): 331-366.
[14] Mulvaney, Paul. "Surface plasmon spectroscopy of nanosized metal particles." Langmuir 12.3 (1996): 788-800.
[15] Schill, Felix, et al. "Visible spectrum optical communication and distance sensing for underwater applications." Proceedings of ACRA. 2004.
[16] Shen, Liang, et al. "A Self-Powered, Sub-nanosecond-Response Solution-Processed Hybrid Perovskite Photodetector for Time-Resolved Photoluminescence-Lifetime Detection." Advanced Materials 28.48 (2016): 10794-10800.
[17] Auston, D. H., et al. "An amorphous silicon photodetector for picosecond pulses." Applied Physics Letters 36.1 (1980): 66-68.
[18] Salamin, Yannick, et al. "100 GHz plasmonic photodetector." ACS photonics 5.8 (2018): 3291-3297.